A 3-D Magnetic Charge Finite-Element Model of an Electrodynamic Wheel

Jonathan Bird and Thomas A. Lipo, *Life Fellow, IEEE*

University of Wisconsin-Madison, Madison, WI 53706 USA

When a magnetic rotor is both rotated and translationally moved above a conductive, nonmagnetic, guideway eddy currents are induced that can simultaneously create lift, thrust, and lateral forces. In order to model these forces, a 3-D finite-element model with a magnetic charge boundary has been created. The modeling of the rotational motion of magnets by using a fictitious complex magnetic charge boundary enables fast and accurate steady-state techniques to be used. The conductive regions have been modeled using the magnetic vector potential and nonconducting with the magnetic scalar potential. The steady-state model has been validated by comparing it with a Magsoft Flux 3D transient model (without translational velocity) and with experimental results. The 3-D model is also compared with a previously presented 2-D steady-state complex current sheet model.

***Index Terms*—Eddy currents, finite-element method, maglev, magnetic charge.**

I. Introduction

HIGH-SPEED maglev ground transportation vehicles typically use either electromagnetic suspension (EMS) or electrodynamic suspension (EDS) methods. However, the rapid translational motion of magnetic fields past conductors creates an unavoidable magnetic drag force. In order to mitigate this drag force, laminated guideway stator packs are used if EMS is employed [1], [2]. Whilst if EDS methods are used, then some type of null-full coil guideway topology is typically utilized [3]–[5]. However, both such methods greatly add to the track construction costs while still nontrivial drag forces are present [6]. An example of this is shown in Fig. 1.

One means of avoiding these magnetic suspension drag losses is to place magnets on the guideway [7]. However, the cost of doing this for long-distance travel would be astronomical. Another method is to convert the detrimental drag force into a useful propulsive force as well as suspension [8]–[20]. This can be accomplished by rotating the magnetic sources over the guideway rather than translationally moving them. This force creation is analogous to how the wheels of an automobile utilize friction to create traction. A radial magnet embodiment of this electrodynamic wheel (EDW) is illustrated in Fig. 2. In this analysis, a Halbach rotor [21], such as shown in Fig. 3, will be used. The use of the split-sheet guideway configuration shown in Fig. 2 has been studied because this type of topology is capable of creating lateral re-centering forces. This flat split-sheet topology was first proposed by Atherton and Eastham [22], [23] for EDS and earlier by Kolm and Thornton in a curved configuration [24]. A similar double-row loop coil topology has also been proposed by He and Rote [25]. The induced current paths for a split ladder topology are schematically shown in Figs. 4 and 5 for the case of a centered and offset translationally moving magnet. These figures show that the lateral force, F_z, is proportional to the difference between the split-ladder (or split-sheet) currents, i.e., $F_z \propto (I_2 - I_1)$. Thus, the lateral forces fully cancel when the moving magnet is centered.

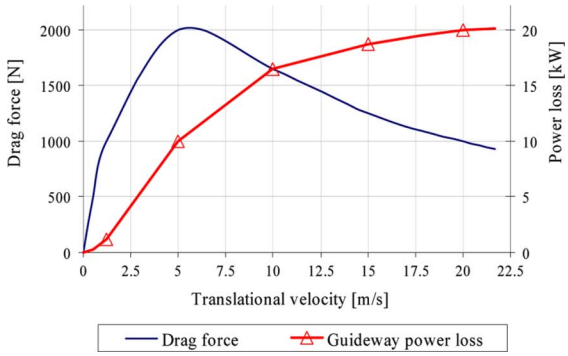

Fig. 1. Experimental drag and guideway power loss for an experimental EDS test-rig used by the General Atomic's urban maglev project [4], [5]. The drag force decreases with speed but the guideway power loss does not.

However, unlike null-flux guideway topologies [3] none of the drag force components cancel, even when a magnet is centered. Although this noncanceling drag is highly undesirable if the magnets are moved only translationally, this topology is very useful for the EDW because large thrust (and lift forces) will be generated when the EDW is centered. Like with other inductive devices, the EDW's lift, thrust, and lateral forces are dependent on a slip speed, defined as

$$s = \omega_m r_o - v_x \quad [\text{ms}^{-1}] \tag{1}$$

where

ω_m = rotor mechanical angular velocity [rads^{-1}]
r_o = rotor outer radius [m]
v_x = translational velocity [ms^{-1}].

Previously, a 2-D EDW model, that used a Halbach rotor, was studied by using a steady-state current-sheet model and many salient characteristics were determined [18], [19]. However, a 2-D model cannot enable lateral z-axis forces to be assessed nor can a 2-D model account for field variations along the z-axis or the finite conducting sheet width. Therefore, in order to fully characterize the performance of an EDW in terms of lift, thrust, and lateral force capabilities and efficiency, lift-to-weight, and lift-to-thrust metrics, a 3-D model is needed. Unfortunately, the straight extension of a 2-D current-sheet model to 3-D does not correctly model the 3-D fields and moreover it will

Digital Object Identifier 10.1109/TMAG.2007.911597

Color versions of one or more of the figures in this paper are available online at http://ieeexplore.ieee.org.

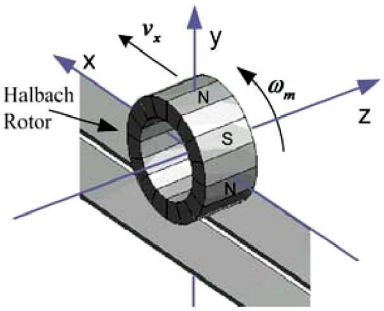

Fig. 2. An electrodynamic wheel over a split-sheet guideway.

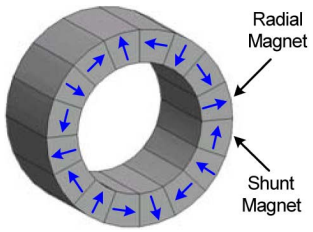

Fig. 3. A four pole-pair Halbach rotor.

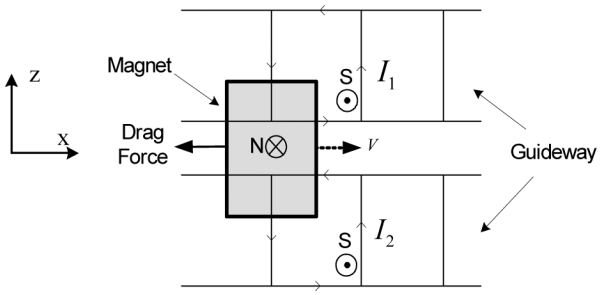

Fig. 4. Induced current path in split-guideway ladder topology when vehicle magnet is at the lateral center position. Only lift and drag forces are created since the guidance forces cancel, i.e., $I_2 = I_1$.

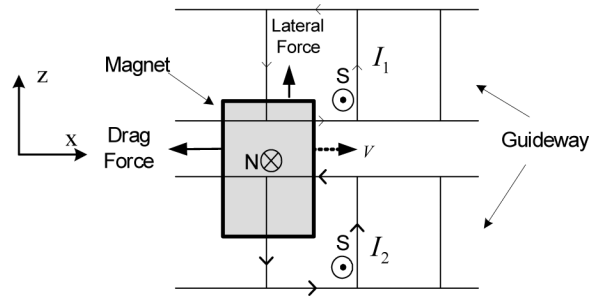

Fig. 5. Induced current path in split-guideway ladder topology when vehicle magnet is laterally offset from the center. In this case guidance, lift, and drag force are created $(I_2 > I_1)$.

be computationally inefficient. While most commercial 3-D transient finite-element and boundary element packages can model 3-D eddy-current problems with motion, they usually use a moving boundary mesh technique [26], [27], although there are exceptions, such as software by Rodgers [28]. Fuji *et al.* used a moving boundary mesh technique to investigate the characteristics of axially rotating magnetic wheels over aluminum and copper sheets [11]–[14]. But this analysis did not also include the translational motion effects. The modeling of the translational motion by moving the guideway or source becomes impractical when high translational speeds and large problem regions need to be analyzed because the guideway must be very long in order to reach steady-state conditions.

Other researches have previously used dynamic circuit methods [29]–[39] also sometimes called generalized machinery theory [40], and mesh-matrix methods [41]–[43] to analyze similar 3-D problems. These formulations model the guideway in terms of a set of magnetically coupled space and time-dependent lump-parameter circuits governed by a set of differential equations in matrix form. When sheet conductors are considered, the guideway sheet is divided up into a grid of coupled lump-parameter circuits. However, such models inherently ignore the skin effect and in the authors' experience this leads to severe accuracy limitations since the skin effect greatly influences the lumped parameter inductance and resistance values [44].

Therefore, due to lump-parameter guideway model shortcomings, a 3-D steady-state EDW finite-element model has been developed. It is beneficial to first determine the steady-state characteristics of an EDW since the uses of a steady-state model can enable potential designs to be assessed far more rapidly than with transient techniques. Therefore, in order to reduce the computational time and memory requirements while still explicitly modeling the rotor magnetic fields, the rotating magnets have been modeled by using a fictitious complex magnetic charge boundary. The use of a magnetic charge boundary enables the nonconducting regions to be modeled using the magnetic scalar potential. The conductive regions have been modeled using the magnetic vector potential and the translational motion was accounted for by including the Minkowski transformation in the guideway formulation [45].

In this paper, the developed 3-D finite-element magnetic charge model is compared with a Magsoft Flux 3D transient finite-element model (with no translation) and with experimental results. It is also compared with a previously developed 2-D model [18].

II. Partial Differential Equation Formulation

The applicable quasi-static field equations are [46]

$$\nabla \times \mathbf{E} = -\frac{\partial \mathbf{B}}{\partial t} \tag{2}$$

$$\nabla \times \mathbf{H} = \mathbf{J} \tag{3}$$

$$\nabla \cdot \mathbf{B} = 0 \tag{4}$$

$$\mathbf{J} = \sigma(\mathbf{E} + \mathbf{v} \times \mathbf{B}) \tag{5}$$

$$\mathbf{B} = \mu_0(\mathbf{H} + \mathbf{M}) \tag{6}$$

where

$$\sigma = \text{conductivity of track} \quad [\text{Sm}^{-1}]$$
$$\mu_0 = \text{permeability of free space} \quad [\text{Hm}^{-1}]$$
$$\mathbf{v} = \text{translational velocity} \quad [\text{ms}^{-1}]$$
$$\mathbf{M} = \text{magnetization vector} \quad [\text{Am}^{-1}].$$

The guideway material is assumed to be made of linear, homogeneous, simply connected, nonmagnetic material, such as aluminum. And the guideway is assumed to move translationally

rather than the rotor magnets. Re-expressing (2)–(6) in terms of the magnetic vector potential $\mathbf{A}$ and electric scalar potential, V

$$\mathbf{E} = -\frac{\partial \mathbf{A}}{\partial t} - \nabla V \quad [\mathrm{Vm}^{-1}] \tag{7}$$

$$\mathbf{B} = \nabla \times \mathbf{A} \quad [\mathrm{T}] \tag{8}$$

one obtains [18]

$$\nabla \times (\nabla \times \mathbf{A}) = \mu_0 \sigma \left(\mathbf{v} \times (\nabla \times \mathbf{A}) - \frac{\partial \mathbf{A}}{\partial t} - \nabla V \right) + \mu_0 \nabla \times \mathbf{M} \tag{9}$$

and since $\nabla \cdot \mathbf{J} = 0$ then

$$\nabla \cdot \left(\mathbf{v} \times (\nabla \times \mathbf{A}) - \frac{\partial \mathbf{A}}{\partial t} - \nabla V \right) \sigma = 0. \tag{10}$$

Using the identity

$$\nabla \times (\nabla \times \mathbf{A}) = \nabla(\nabla \cdot \mathbf{A}) - \nabla^2 \mathbf{A} \tag{11}$$

and the Coulomb gauge $\nabla \cdot \mathbf{A} = 0$, (9) and (10) reduce to

$$\nabla^2 \mathbf{A} = \mu_0 \sigma \left(\frac{\partial \mathbf{A}}{\partial t} + \nabla V - \mathbf{v} \times (\nabla \times \mathbf{A}) \right) - \mu_0 \nabla \times \mathbf{M} \tag{12}$$

$$\nabla \cdot (\mathbf{v} \times (\nabla \times \mathbf{A}) - \nabla V) \sigma = 0. \tag{13}$$

The use of (12) and (13) in the air and track region is known as the $\mathbf{A}V - \mathbf{A}$ formulation [28], [47]–[52]. The electric scalar potential in (12) and (13) cannot be removed by using the $\mathbf{A}^*$ method [53], [54] because if ∇V is removed then trying to impose $\mathbf{J} \cdot n = 0$ on the boundary when $\mathbf{v} \times (\nabla \times \mathbf{A}) \neq 0$ will give erroneous results [55]. However, Roger showed that the electric scalar potential can be expressed as

$$V = \mathbf{v} \cdot \mathbf{A} \quad [\mathrm{V}]. \tag{14}$$

Thereby leading to a formulation in terms of $\mathbf{A}$ alone [18], [28], [45], [48], [56]

$$\nabla^2 \mathbf{A} = \mu_0 \sigma \left(\frac{\partial \mathbf{A}}{\partial t} + (\mathbf{v} \cdot \nabla)\mathbf{A} \right) - \mu_0 \nabla \times \mathbf{M}. \tag{15}$$

Alternatively, (15) can be derived by expressing (12) and (13) in the fixed (Lagrangian) laboratory reference frame when the velocity, $\boldsymbol{v}$, is zero [57]. In this case

$$\frac{\partial \mathbf{A}}{\partial t} = \frac{d\mathbf{A}}{dt} \tag{16}$$

and therefore the $\mathbf{A}^*$ model can be used [53], giving

$$\nabla^2 \mathbf{A}^* = \mu_0 \sigma \frac{d\mathbf{A}^*}{dt} - \mu_0 \nabla \times \mathbf{M} \tag{17}$$

where

$$\frac{d\mathbf{A}^*}{dt} = \frac{d\mathbf{A}}{dt} + \nabla V. \tag{18}$$

If this model is now converted into the Eulerian frame [57], [58] in which the position is a function of time, then

$$\frac{d\mathbf{A}^*}{dt} = \frac{\partial \mathbf{A}^*}{\partial t} + (\mathbf{v} \cdot \nabla)\mathbf{A}^*. \tag{19}$$

Substituting (19) back into (17) yields (15). Rodgers was the first to propose using (15) for 3-D eddy-current analysis [45] However, this 3-D formulation was used much earlier by linear induction motor researches [59].

A. Conducting Guideway Region

If a steady-state solution can be obtained in which

$$\mathbf{A}(x, y, z, t) = \mathbf{A}(x, y, z) e^{j\omega_e t} \quad [\mathrm{Wbm}^{-1}] \tag{20}$$

where $\omega_e =$ electric angular velocity, then assuming the translational velocity only has an x-component allows the conducting region, (15), to be expressed as

$$\nabla^2 \mathbf{A} = \mu_0 \sigma \left(j\omega_e \mathbf{A} + v_x \frac{\partial \mathbf{A}}{\partial x} \right). \tag{21}$$

B. Nonconducting Region

Within the nonconducting regions the magnetic flux density is expressed in terms of the magnetic scalar potential, ϕ, as

$$\mathbf{B} = -\mu_0 \nabla \phi \quad [\mathrm{T}]. \tag{22}$$

The formulation in terms of the magnetic scalar potential alone is then

$$\nabla^2 \phi = 0. \tag{23}$$

It is well known that the field of a magnet can be modeled using a fictitious magnetic volume charge density, ρ_m and surface charge density, ρ_{ms} defined as [46]

$$\rho_m(r, \theta, z) = -\nabla \cdot \mathbf{M} \quad [\mathrm{Am}^{-2}] \tag{24}$$

$$\rho_{\mathrm{ms}}(x, y, z) = \mathbf{M} \cdot \mathbf{n} \quad [\mathrm{Am}^{-1}]. \tag{25}$$

If $\mathbf{M}$ is assumed to be uniform within the magnets, the charge density exists only on the surface of the radial and azimuthally magnetized magnets [46], as illustrated in Fig. 6. Thus, the magnetization surface charge can be defined as

$$\rho_{\mathrm{ms}} = \begin{cases} M_0 & \text{on the top magnet face} \\ -M_0 & \text{on the bottom magnet face} \\ 0 & \text{on the side walls} \end{cases} \quad [\mathrm{Am}^{-1}]. \tag{26}$$

The modeling of the rotational motion of the Halbach magnet pieces using the magnetic charge model, as shown in Fig. 6, will require the use of a rotating moving boundary mesh. However, the use of rotation can be avoided altogether if the magnetic charge is assumed to exist only on the outer surface of the rotor, such as illustrated in Fig. 7. As only the field outside the surface of the magnets is of interest, this is a reasonable proposition. Also, in the same way that complex steady-state current sheets are often employed to avoid transient modeling of machines [18], [59], a complex magnetic charge sheet can be used to model the rotation of the magnets. In which case, for a Halbach rotor with P pole pairs a complex sinusoidal field can be generated by using

$$\rho_{\mathrm{ms}}(r_0, \theta, z) = \rho_p e^{jP\theta} \quad [\mathrm{Am}^{-1}]. \tag{27}$$

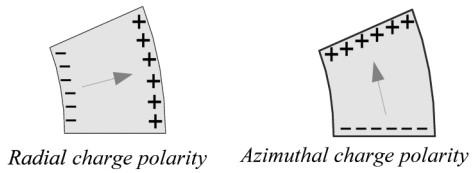

Fig. 6. Illustration of the radial and azimuthal fictitious surface magnet charge for a radial magnetized and azimuthally magnetized magnet.

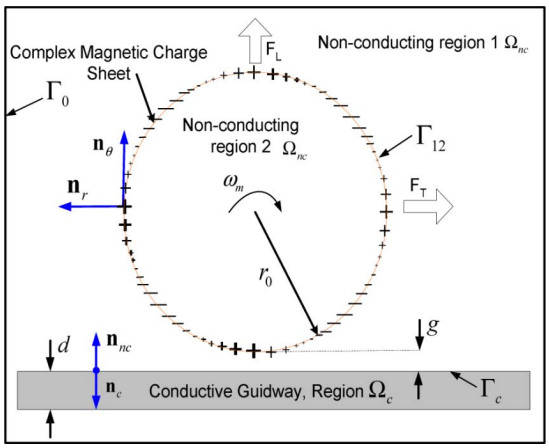

Fig. 7. A 2-D schematic of the electrodynamic wheel magnetic charge sheet model.

By making the charge sheet complex, the rotational motion of the magnets can be modeled using steady-state methods. The rotor mechanical frequency will then be related to the electrical guideway frequency by

$$\omega_m = \frac{\omega_e}{P} \quad [\text{rads}^{-1}] \tag{28}$$

where P is the number of pole pairs.

III. Boundary Conditions

A. Magnetic Charge Sheet Boundary Conditions

Analogous to electric charge, the necessary boundary condition for the magnetic charge sheet between the two nonconducting regions shown in Fig. 7 will be [60]

$$\mathbf{n}_r \cdot (\nabla\phi_1 - \nabla\phi_2) = \rho_{\text{ms}}(r_0, \theta, z) \text{ on } \Gamma_{12} \quad [\text{Am}^{-1}] \tag{29}$$

where ϕ_1 and ϕ_2 are the scalar potential values in regions 1 and 2. Assuming that the rotor magnets are radially magnetized and the field is highly repetitive, then the charge sheet will only have a field component normal to the surface region [46]. In such a case, the entire region behind the magnet is superfluous. This leads to the reduced problem region shown in Fig. 8 in which the rotor field symmetry enables only half of the rotor to be modeled in steady-state. In this case, the magnetic charge boundary condition can be expressed as

$$-\mathbf{n}_r \cdot \nabla\phi_1 = \rho_{\text{ms}}(r_0, \theta, z) \text{ on } \Gamma_1 \quad [\text{Am}^{-1}]. \tag{30}$$

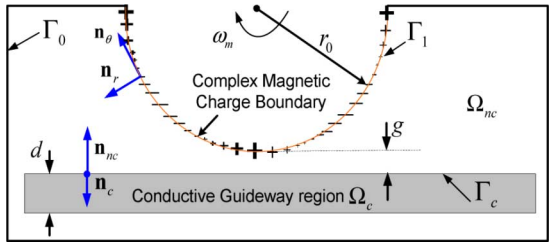

Fig. 8. A half rotor 2-D schematic of the electrodynamic wheel magnetic charge boundary model.

Since the left side of (30) is the radial magnetic field intensity, the value of the magnetic charge sheet on the boundary is simply

$$\rho_{\text{ms}} = H_r(r_0, \theta, 0) \text{ on } \Gamma_1 \quad [\text{Am}^{-1}]. \tag{31}$$

More generally, the boundary condition can be expressed as a complex Fourier series

$$H_r(r_0, \theta, 0) = \sum_{n=0}^{\infty} H_n e^{jnP\theta} \text{ on } \Gamma_1 \quad [\text{Am}^{-1}]. \tag{32}$$

The charge density on the surface of the rotor is uniformly distributed along the z-axis. Thus, only the radial field component at $z = 0$ is required. Therefore, knowing only the 2-D form of a rotor field enables the 3-D field to be accurately modeled when using the magnetic charge sheet concept. Unlike using a 2-D current sheet, the 2-D magnetic charge sheet correctly models all three Halbach field components in 3-D and naturally accounts for the field variation along the z-axis as confirmed in Section IV.

The Dirichlet boundary condition is applied on the nonconducting and nonmagnetic boundaries:

$$\phi_1 = 0, \text{ on } \Gamma_0. \tag{33}$$

B. Conducting and Nonconducting Boundary Conditions

The necessary magnetic boundary conductions on the conducting boundary, Γ_c, are

$$\mathbf{H} \times \mathbf{n}_c - \nabla\phi \times \mathbf{n}_{\text{nc}} = \mathbf{0} \tag{34}$$

$$\mathbf{n}_c \cdot \mathbf{H} - \mathbf{n}_{\text{nc}} \cdot \nabla\phi = 0 \tag{35}$$

where the coupling normal vectors, $\mathbf{n}_{\text{nc}}$ and $\mathbf{n}_c$, are in opposite directions (see Fig. 8). As the conducting region is linear the Coulomb gauge is implied by (21), [61], [62]. However, in order to ensure the uniqueness of the solution

$$\mathbf{n}_c \cdot \mathbf{A} = 0 \text{ on } \Gamma_c \tag{36}$$

must also be enforced on the conductive boundaries [55], [56], [61]. This is a necessary condition since

$$\int_{\Omega_c} \nabla \cdot \mathbf{A} d\Omega_c = \int_{\text{T}_c} \mathbf{A} \cdot \mathbf{n}_c d\Gamma_c = 0. \tag{37}$$

This additional boundary condition also has the added benefit of setting the normal component of the current on the boundaries to zero ($\mathbf{n}_c \cdot \mathbf{J} = 0$).

IV. The Weak Form for the $\mathbf{A}$-$\boldsymbol{\phi}$ Formulation

By using Green's first identity:

$$w\nabla^2\phi = \nabla \cdot (w\nabla\phi) - \nabla w \cdot \nabla\phi \tag{38}$$

and defining w as the element shape function, the weak form in the nonconducting region, $\Omega_{\rm nc}$, governed by (23) will be [53], [63]

$$0 = \int_{\Omega_{\rm nc}} w\nabla^2\phi d\Omega_{\rm nc} \tag{39}$$

$$= -\int_{\Omega_{\rm nc}} \nabla\phi \cdot \nabla w \cdot d\Omega_{\rm nc} + \int_{\Gamma_c} w\nabla\phi \cdot \mathbf{n}_{\rm nc} d\Gamma_c. \tag{40}$$

Within the conducting guideway, the three vector potential components of (21) will have the same weak form. For instance, the y-component will be

$$\int_{\Omega_c} N_y \left[\nabla^2 A_y - \mu_0\sigma\left(v_x\frac{\partial A_y}{\partial x} + j\omega_e A_y\right)\right] d\Omega_c = 0 \tag{41}$$

where N_y is the y-component element shape function. Using Green's identity (41) can be rewritten as

$$-\int_{\Omega_c} \nabla N_y \cdot \nabla A_y d\Omega_c - \mu_0\sigma \int_{\Omega_c} N_y \left(v_x\frac{\partial A_y}{\partial x} + j\omega_e A_y\right) d\Omega_c + \int_{\Gamma_c} N_y(\nabla A_y \cdot \mathbf{n}_c)\, d\Gamma_c = 0. \tag{42}$$

The boundary conditions between the air and guideway regions are coupled using the usual interface conditions [53], [63]. For instance, the boundary term in (40) is

$$\int_{\Gamma_c} w\nabla\phi \cdot \mathbf{n}_{\rm nc} d\Gamma_c = -\frac{1}{\mu_0}\int_{\Gamma_c} w(\nabla \times \mathbf{A}) \cdot \mathbf{n}_{\rm nc} d\Gamma_c. \tag{43}$$

While, for example, the y-component of the conducting region boundary condition in (42) together with (36) will be

$$\int_{\Gamma_c} N_y \left[\frac{\partial A_y}{\partial x}\mathbf{n}_{cx} + \left(\frac{\partial A_y}{\partial y} + A_y\right)\mathbf{n}_{cy} + \frac{\partial A_y}{\partial z}\mathbf{n}_{cz}\right] d\Gamma_c = 0 \tag{44}$$

where, for example, $\mathbf{n}_{cx}$ is the x -component normal vector to the conducting boundary region. If (44) is re-expressed in terms of the magnetic scalar potential by using $\nabla \times \mathbf{A} = -\mu_0\nabla\phi$ and $\nabla \cdot \mathbf{A} = 0$, then the conducting boundary conditions for the y-component will be

$$\int_{\Gamma_c} N_y \left[\left(\frac{\partial A_x}{\partial y} - \mu_0\frac{\partial\phi}{\partial z}\right)\mathbf{n}_{cx} - \left(\frac{\partial A_y}{\partial x} + \frac{\partial A_y}{\partial z} - A_y\right)\mathbf{n}_{cy} + \left(\frac{\partial A_z}{\partial y} + \mu_0\frac{\partial\phi}{\partial x}\right)\mathbf{n}_{cz}\right] d\Gamma_c. \tag{45}$$

Analogous equations are obtained for the x- and z-components.

V. Upwinding

Equation (21) contains both a convective and a diffusive contribution. When the convective term dominates, it is well known that spurious numerical oscillatory behavior can result when the Peclet number defined as [56], [64]

$$P_e = \frac{\mu_0\sigma v_x h}{2} \tag{46}$$

exceeds unity. The variable h is the element length in the direction of motion. In order to prevent these numerical inaccuracies, most authors of translational electromagnetic motion problems have used the quadrature-upwind scheme proposed by Hughes [65]. However, Hughes showed that this scheme can suffer from spurious crosswind diffusion effects [66]–[69]. Therefore, based on its success in fluid dynamic analysis the Streamline-upwind Petrov–Galerkin (SUPG) method was implemented. It has been shown to not suffer from many of the numerical inaccuracies present in other upwinding schemes when applied to multidimensional problems. The SUPG method involves using a Petrov–Galerkin method, i.e., choosing a weighting function that does not equal the shape function, $W_i \neq N_i$. For the SUPG method, the weighting function is defined as

$$W_i = N_i + p_i, \quad i = x, y, z. \tag{47}$$

For the case in which there is only one velocity term p_i is

$$p_i = \frac{\alpha h}{2}\frac{v_x}{|v_x|}\frac{\partial N_i}{\partial x} \tag{48}$$

where

$$\alpha = \coth(P_e) - \frac{1}{P_e}. \tag{49}$$

The derivative of the shape function in the weighting function is only necessary when there is a convective velocity term, and is only in the direction of convection. Since the derivate in (48) introduces a discontinues function the Green's function is only used to simplify equations that contain the N_i term. Therefore, the modification to the weighting function will only pertain to the volume region terms. Using (47) as the weighting function in (41) will yield the following equation in place of (42): [70]

$$-\int_{\Omega_c} \nabla N_y \cdot \nabla A_y d\Omega_c - \mu_0\sigma \int_{\Omega_c} W_y \left(v_x\frac{\partial A_y}{\partial x} + j\omega_e A_y\right) d\Omega_c + \int_{\Omega_c} p_y \cdot \nabla^2 A_y d\Omega_c + \int_{\Gamma_c} N_y\,(\nabla A_y \cdot \mathbf{n}_c)\, d\Gamma_c = 0. \tag{50}$$

This weak form equation together with analogous x and z terms and the nonconducting region terms were implemented using FEMLAB 3.1. However, after analyzing a number of problems it has been determined that no spurious field oscillations occur when not using upwinding for the speeds presented in this paper, despite the Pelcet number being greater than 1. Perhaps, as suggested by Chan, these detrimental oscillations depend also on the linear material and boundary conditions [64].

VI. Magnetic Charge Static Field Validation

The magnetic charge rotor model, developed in FEMLAB, is shown in Fig. 9. It was validated by comparing it with a 3-D analytic model of a Halbach rotor derived using Biot–Savart's

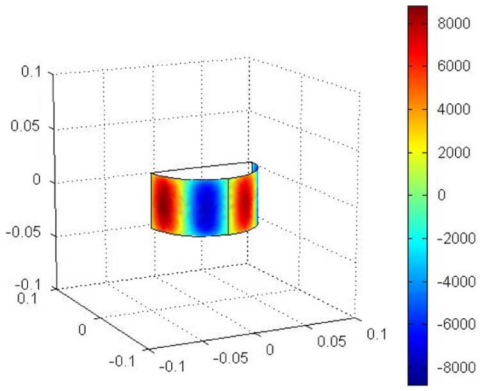

Fig. 9. The value of the magnetic scalar potential [Am^{-2}] on a 4-pole-pair rotor surface using magnetic charge. Due to the rotor symmetry, only half of the rotor has been modeled.

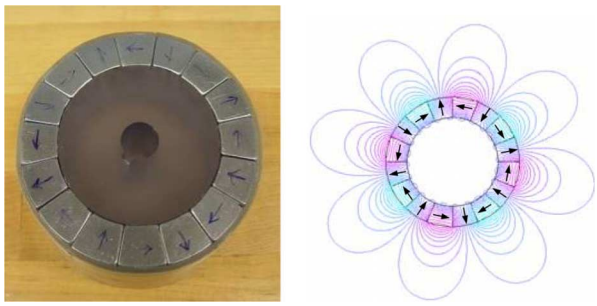

Fig. 10. The 4-pole pair NdFeB Halbach rotor with lexan yoke and sleeve. The magnet thickness was chosen by using 2-D optimization in order to achieve the highest lift-to-weight ratio [18]. Also shown are the vector potential field lines created by the Halbach rotor.

TABLE I
SIMULATION PARAMETERS

Rotor:	outer radius, r_o	50 mm
	inner radius, r_i	34.2 mm
	width, w	50 mm
	magnet B_r (NdFeB)	1.42
	magnet relative permeability	1.055
	pole-pairs, P	4
Guideway:	conductivity (Al)	2.459×10^7 Sm^{-1}
	guideway sheet width	77 mm
	guideway thickness, t	6.3 mm
	air-gap between rotor and guideway	8 mm

law [44], and to an experimentally built Halbach rotor, shown in Fig. 10. The calculated vector potential field lines created by the rotor is also shown in Fig. 10. The Halbach rotor parameters are given in Table I.

An illustration of the field comparison between the magnet charge model, experimental results, analytically calculated value, and a previously presented 2-D model [18] is shown in Figs. 11 and 12. The experimental value is approximately 10% lower than predicted. The peak field value significantly reduces near the edges of the rotor and although the 2-D field model gives close results at the center it overestimates the radial and azimuthal field near the rotor edges. The magnetic charge sheet accurately and naturally accounts for all the field components

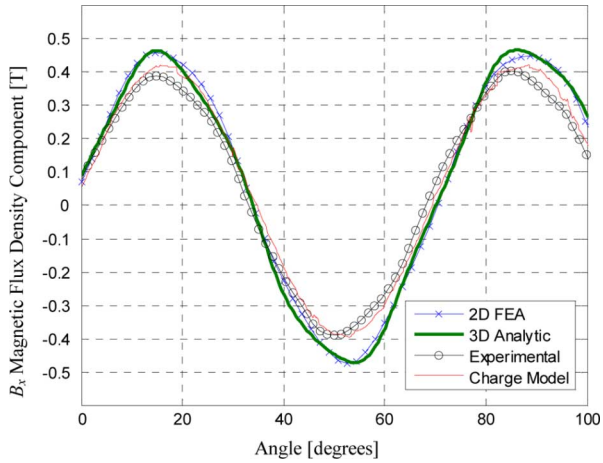

Fig. 11. Comparison between 2-D finite-element model, 3-D analytic model, magnetic charge sheet model and experimental results of the Halbach rotor for the x-component of the magnetic flux density, B_x, at $r = 57$ mm, $z = 0$ mm.

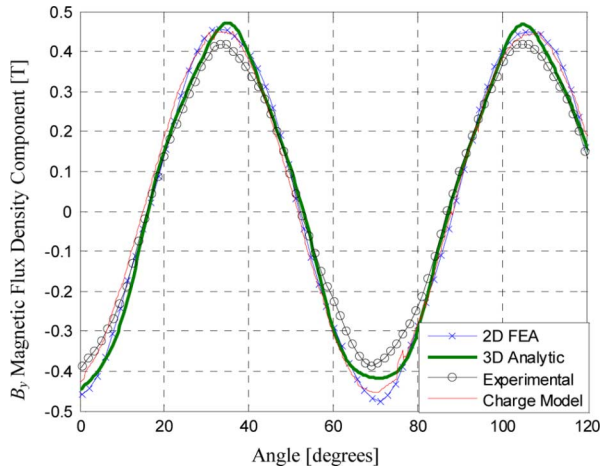

Fig. 12. Comparison between 2-D finite-element model, 3-D analytic model, magnetic charge sheet model, and experimental results of the Halbach rotor for the y-component of the magnetic flux density, B_y, at $r = 57$ mm, $z = 0$ mm.

along the z-axis, as confirmed by the z-component comparison shown in Fig. 13.

VII. STEADY-STATE CHARGE SHEET MODEL COMPARISON

Using the parameters given in Table I, a steady-state $\mathbf{A}$-ϕ charge model, shown in Fig. 14, was developed in FEMLAB v3.1. The rotor was centered over a single 77-mm-wide conducting guideway sheet. The forces were evaluated using both the Lorentz force and Maxwell's stress tensor method. For instance, the thrust force was calculated from

$$F_x = \frac{1}{2}\mathrm{Re}\left(\int_{\Omega_c}(J_y B_z^* - J_z B_y^*)d\Omega_c\right) \quad [\mathrm{N}] \qquad (51)$$

$$= \iint_S \mathrm{Re}\left(\frac{\partial\phi}{\partial y}\right)\mathrm{Re}\left(\frac{\partial\phi}{\partial x}\right)dS. \qquad (52)$$

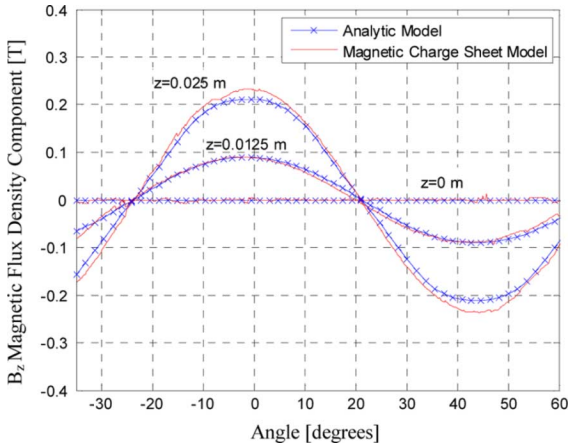

Fig. 13. The z-component of the magnetic flux density at three different z-axis locations, at $r = 57$ mm.

The star superscript denotes conjugation. The lift force is

$$F_y = \frac{1}{2}\mathrm{Re}\left(\int_{\Omega_c} (J_x B_z^* - J_z B_x^*)\, d\Omega_c\right) \quad [\mathrm{N}] \tag{53}$$

$$= \frac{1}{2}\iint_S \left(\mathrm{Re}\left(\frac{\partial\phi}{\partial y}\right)^2 - \mathrm{Re}\left(\frac{\partial\phi}{\partial x}\right)^2 - \mathrm{Re}\left(\frac{\partial\phi}{\partial z}\right)^2\right) dS \tag{54}$$

and the lateral force

$$F_z = \frac{1}{2}\mathrm{Re}\left(\int_{\Omega_c} (J_x B_y^* - J_y B_x^*) d\Omega_c\right) \quad [\mathrm{N}] \tag{55}$$

$$= \iint_S \mathrm{Re}\left(\frac{\partial\phi}{\partial y}\right)\mathrm{Re}\left(\frac{\partial\phi}{\partial z}\right) dS. \tag{56}$$

The surface integral was evaluated over a surface region, S, between the rotor and guideway, as illustrated in Fig. 15. The guideway power loss was computed by using [46]

$$P_{\mathrm{Loss}} = \frac{1}{2\sigma}\int_{\Omega_c} (|J_x|^2 + |J_y|^2 + |J_z|^2)\, d\Omega_c \quad [\mathrm{W}]. \tag{57}$$

While the rotor output torque was computed from

$$T = \frac{P_{\mathrm{Input}}}{\omega_m} \quad [\mathrm{Nm}] \tag{58}$$

where

$$P_{\mathrm{Input}} = P_{\mathrm{Loss}} + F_x v_x \quad [\mathrm{W}]. \tag{59}$$

In order to validate the steady-state $\mathbf{A}$-ϕ model, it was first compared with a transient Magsoft Flux 3D Halbach rotor model shown in Fig. 16 and a steady-state magnetic charge $\mathbf{A}$-V-ϕ model in addition to a previously presented 2-D current sheet model [18]. These four model comparisons are shown in Figs. 17, 18, and 19 for the thrust, lift, and guideway power loss. The Magsoft model used the $\mathbf{T}$-ψ formulation [26], [71], [72]. The $\mathbf{A}$-V-ϕ model, in which the scalar potential is retained was also developed in FEMLAB in order to provide an additional model and performance comparison. No translational motion was present because Magsoft Flux 3D cannot model both simultaneous 3-D transient rotational and translational motion. The comparison immediately shows that the 2-D current sheet model overestimates the forces and guideway losses by approximately 20% while the other three models give close results. The comparison also showed the time saving achieved by using the steady-state model. For instance, when using an Intel Xeon 5130 processor with 4GB of RAM the transient simulation at 6000RPM took 9097 s to reach steady-state conditions, whilst the steady-state $\mathbf{A}$-ϕ model completed the simulation in 435 s.

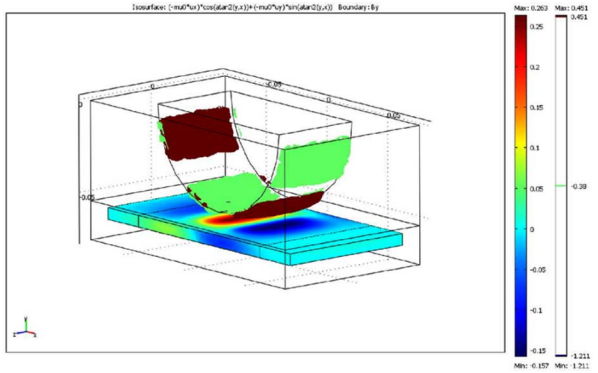

Fig. 14. B_x Magnetic flux density [T] component on the surface of the guideway and B_r iso-surface plot in the air region for the $\mathbf{A}$-ϕ magnetic charge model for $\omega_m = 3000$ RPM, $s = 0.7$ ms^{-1}, $v_x = 15$ ms^{-1}.

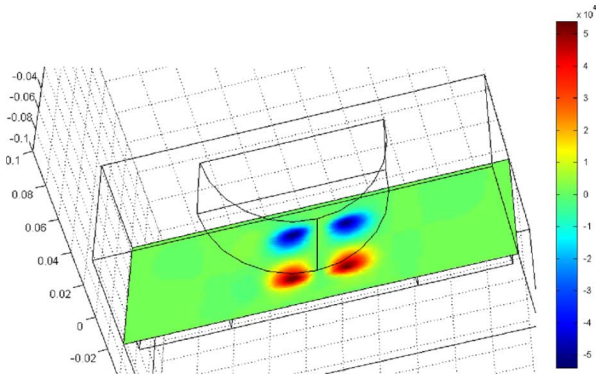

Fig. 15. The surface region, S, within the air-gap used to compute the thrust, lift, and lateral force. The surface color map shown is for the lateral force density which sums to zero since the EDW is at the center of the guideway.

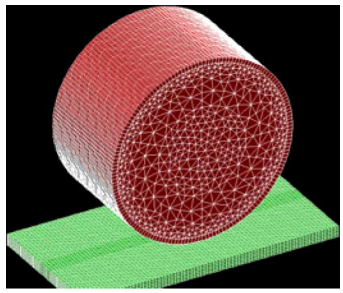

Fig. 16. An example of mesh used by the transient Magsoft Flux 3-D model.

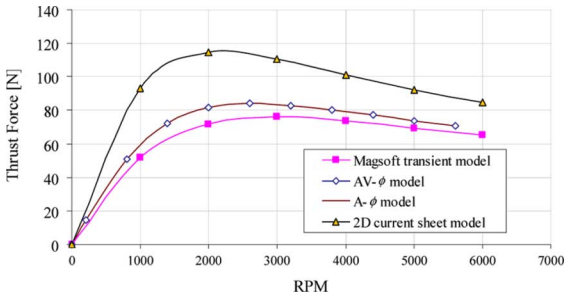

Fig. 17. Thrust force comparison.

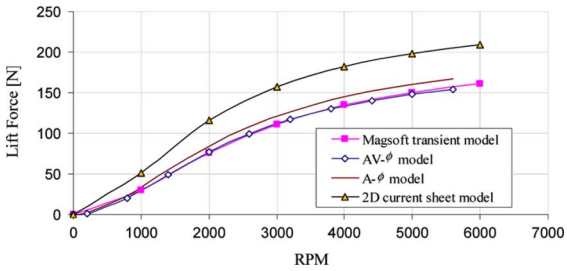

Fig. 18. Lift force comparison.

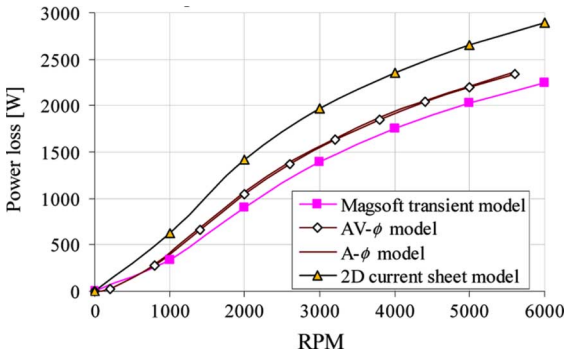

Fig. 19. Guideway power loss comparison.

VIII. Steady-State Charge Model Compared with Experimental Results

In order to validate the effect of both the translational and rotational motion the experimental setup shown in Figs. 20 and 21 was used. The setup parameters are shown in Table II. The forces were measured by holding the "vehicle," shown in Fig. 20, stationary while the EDW rotated and the guideway moved below it. The aluminum guideway is a 1.2 m diameter wheel composed of two 77 mm aluminum sheets separated by 2 mm and 6.3 mm thick. The complete experimental setup showing the guideway wheel and "vehicle" above the guideway wheel is shown in Fig. 21. The induction machine and controller in the foreground were used only for braking purposes in order to keep the guideway translational velocity constant. The EDW was driven by two brushless dc motors with sensor-less controllers. The top cross section of the guideway wheel can be seen in Fig. 20. It is envisaged that future versions will use an integrated motor above the EDW to rotate the EDW. Four load cells measured the lift force, two load cells at the front measured the thrust force, while four load cells could measured

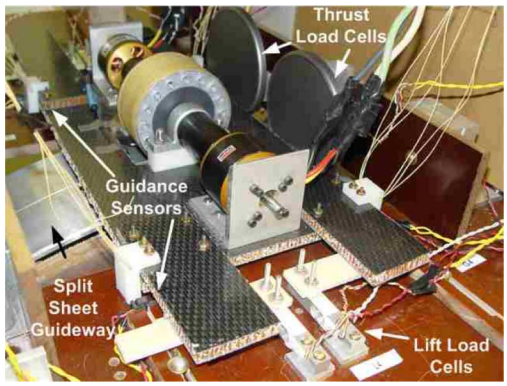

Fig. 20. Electrodynamic wheel with drive motors and some load cells shown. Also visible is the top of the split-sheet aluminum guideway wheel.

Fig. 21. Experimental setup showing guideway wheel.

TABLE II
Experimental Parameters

Rotor:	magnet outer radius, r_o	50 mm± 0.05 mm
	inner radius, r_i	34.2 mm
	width, w	50 mm
	magnet (NdFeB), B_r	1.42T
	pole pairs, P	4
	sleeve thickness	2.6 mm ± 0.1 mm
Guideway:	radius	600 mm ± 0.5 mm
	conductivity (Al)	2.459×10^7 Sm^{-1} [73]
	single sheet width	77 mm
	split sheet gap	2 mm
	Thickness, d	6.3mm
	electrical airgap, g	9.5 mm
	'vehicle mass'	4.8 kg

the lateral forces. A Kevlar fiber rotor sleeve (in yellow) was added to improve the rotor sleeve peak hoop stress capability. The thrust and lift forces were measured separately in order to try and ensure the air-gap stayed fixed during measurements. The lift force was measured by affixing the vehicle to the lift sensors. While the thrust and lateral forces were measured by allowing the "vehicle" to slide only horizontally and lateral.

The effect of the track curvature has been neglected by the calculations. However, this does not greatly affect the experimental results because the guideway wheel curvature is so great

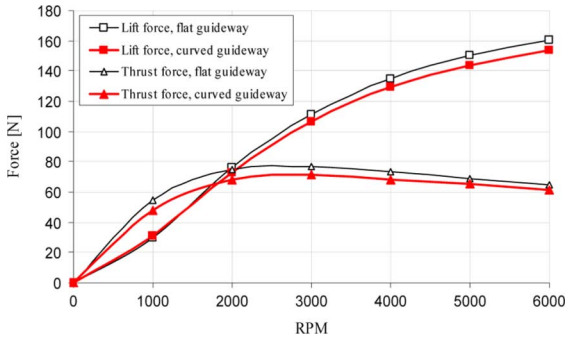

Fig. 22. The effect of the guideway curvature on force when the translational velocity is zero. The Magsoft simulation parameters are shown in Table I.

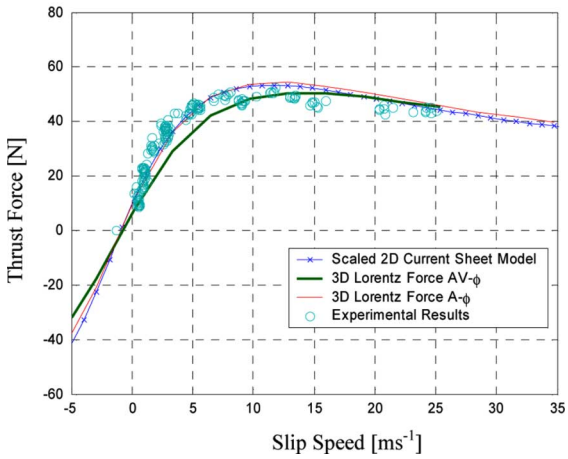

Fig. 23. Thrust force comparison for a 5 ms^{-1} translational velocity.

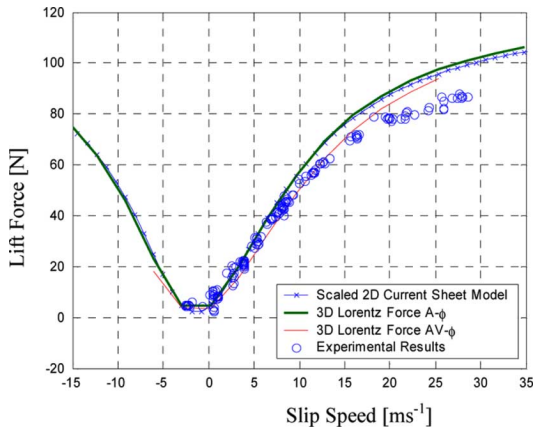

Fig. 24. Lift force comparison for a 5 ms^{-1} translational velocity.

relative to the EDWs. This is confirmed by the Magsoft simulation results shown in Fig. 22 and the experimental results.

A. *Single Sheet Guideway Force Comparison*

The steady state $\mathbf{A}$-ϕ and $\mathbf{A}$-V-ϕ models were first compared with experimental results in which the EDW was rotated over the center of just one 77-mm-wide moving aluminum sheet. This also enabled the previously developed 2-D current sheet model to be assessed. The comparison between the experimental and calculated results for two different translational speeds are

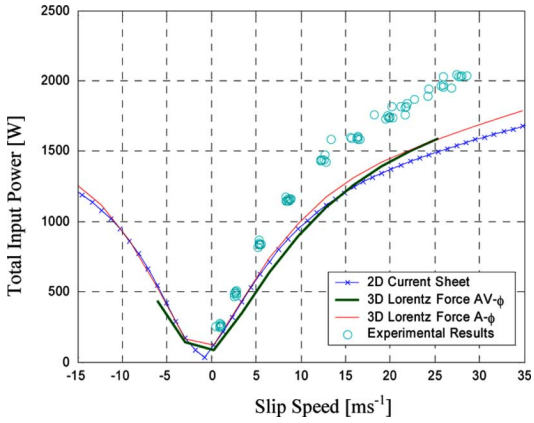

Fig. 25. Total input power, P_{input} for a 5 ms^{-1} translational velocity. The input power was measured at the input to the drive motors' converters. The difference of approximately 20% between the calculated and experimental value is believed to be due to the power loss in the drive motors and converter; both of which are not accounted for by the calculated value.

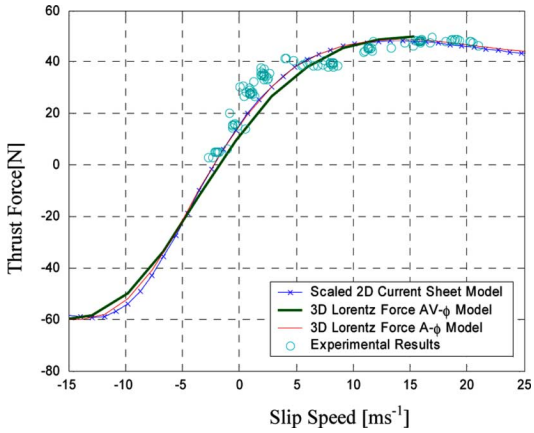

Fig. 26. Thrust force comparison for a 15 ms^{-1} translational velocity.

shown in Figs. 23–27. In most cases, the EDW was rotated up to 6500 RPM. The controllers were not capable of handling regenerative braking; therefore, only experimental thrust forces are shown. The peak B_r used by the models was reduced by 10% in order to agree with the measured field values shown earlier. After this modification, all three models were within approximately 10% of the experimental force results. The $\mathbf{A}$-V-ϕ had comparable accuracy to the $\mathbf{A}$-ϕ model but the mesh had to be made much finer in order to converge on the same result.

The large difference between measured and calculated total input power is believed to be due to the measured power including the EDW drive motor and converter losses. The greatest source of experimental error appears to have been introduced by guideway wheel and EDW airgap variations introduced by vibrations and the guideway being out-of-round. For example, at 6000 RPM and $v_x = 5$ ms^{-1}, a $+1$ mm change in the air gap introduces a 16% and 15% reduction in the lift and thrust force, respectively.

B. *Split-Sheet Guideway Force Comparison*

The experimental results were then compared with the $\mathbf{A}-\phi$ split-sheet magnetic charge model, shown in Figs. 28 and 29.

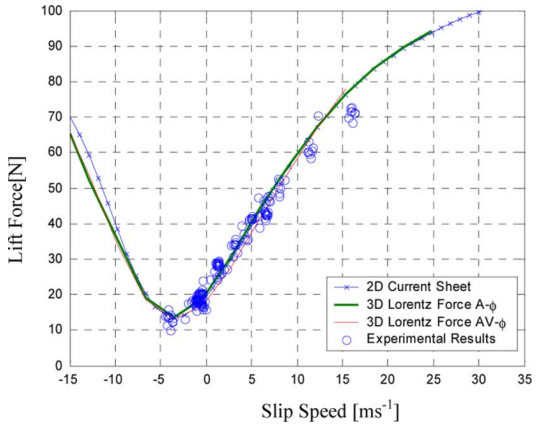

Fig. 27. Lift force comparison for a 15 ms^{-1} translational velocity.

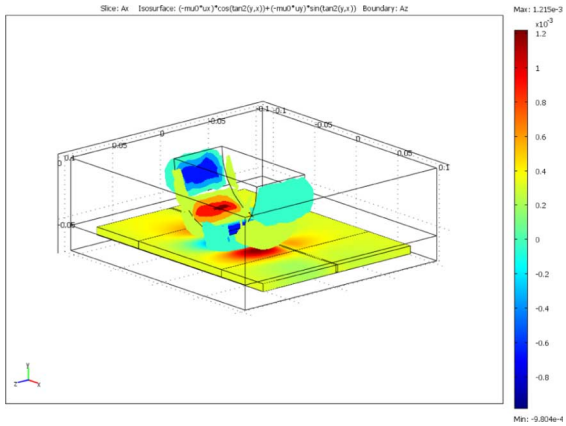

Fig. 28. B_r iso-surface plot of the split-sheet steady-state complex magnetic charge model with A_z values shown on the guideway surface. A 5 ms^{-1} translational velocity and a 3000 RPM was used (10.7 ms^{-1} slip speed).

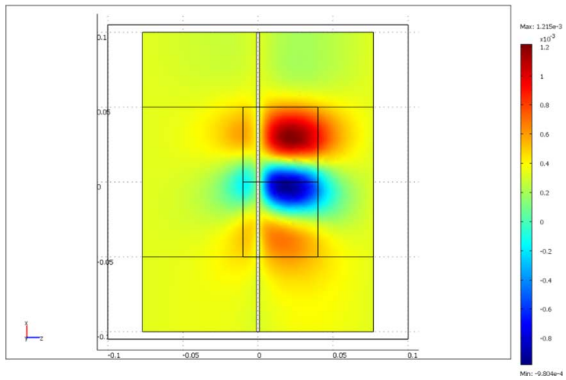

Fig. 29. Magnetic vector potential on the surface of the guideway. For a 5 ms^{-1} translational velocity at 3000 RPM and with a 15 mm lateral offset. The trailing field induced in the guideway is evident.

The split region between the conducting sheets used the magnetic scalar potential formulation. The comparison between the experimental and calculated thrust and lift forces at two different translational velocities when the EDW is at the center of the split-sheet guideway is shown in Figs. 30 and 31. While Fig. 32 shows the input power comparison for the 15 ms^{-1} translational case. Lastly, Fig. 33 confirms the predicted re-centering lateral

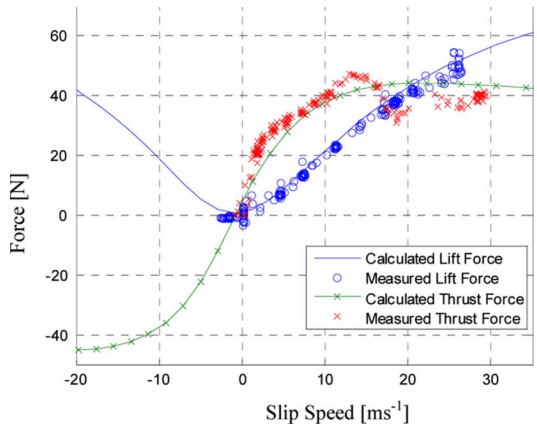

Fig. 30. Thrust and lift force comparison when the EDW is at the center of the split-sheet guideway. The translational velocity is 5 ms^{-1}.

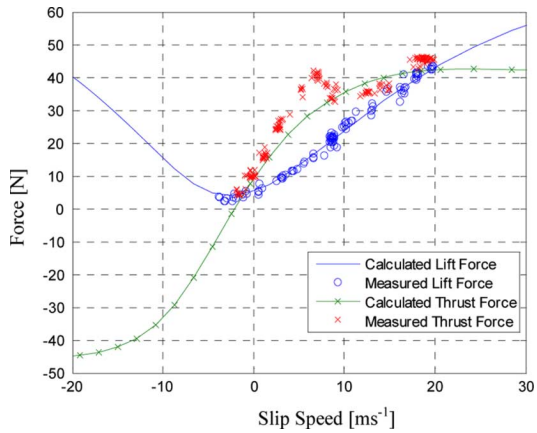

Fig. 31. Thrust and lift force comparison when the EDW is at the center of the split-sheet guideway and the translational velocity is 15 ms^{-1}.

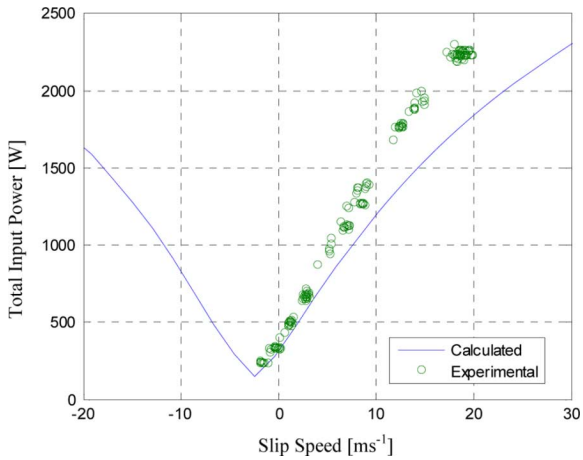

Fig. 32. Total input power for 15 ms^{-1} translational velocity. The difference of approximately 20% between the calculated and experimental values is believed to be due to the loss in the drive motors and converter.

forces when the EDW is laterally offset. Some difficulty was encountered when trying to measure the thrust force whilst keep the air gap fixed. Overall, good agreement has been obtained between the experimental and calculated results.

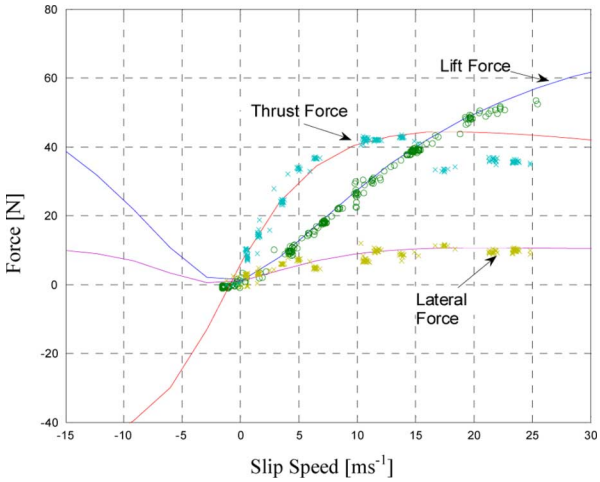

Fig. 33. Thrust, lift, and lateral force comparison when the EDW is 15mm off-center from the split-sheet center. The translational velocity is 5 m/s.

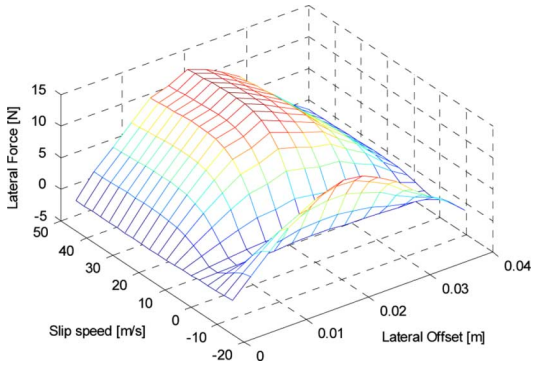

Fig. 34. Lateral re-centering force versus slip velocity and lateral rotor offset for a 5 ms^{-1} translational velocity.

IX. Discussion

The use of a split-sheet guideway can potentially create significant lateral re-centering forces. Fig. 34 more clearly shows this relationship at different slip values for the experimental setup. The cost incurred by creating lateral restoring forces is a reduction in the lift force, and to a lesser extent thrust compared to when the EDW is over one sheet, as shown in Figs. 35–37. The challenge, therefore, is to develop a suitable design which will create sufficient lift and thrust forces. If a Halbach rotor made of NdFeB magnets is to be used, then perhaps a lower number of poles will need to be used in order to create a sufficient lift-to-weight ratio and multiple EDW in series will be needed in order to achieve sufficiently high thrust performance [19].

X. Conclusion

The modeling of the simultaneous high-speed rotational and translational motion of magnets above an aluminum track is difficult to model using transient techniques and is relatively time consuming. However, modeling the rotation of magnets using a complex magnetic charge boundary and using the convective-diffusion equation to account for translational motion enables a "fast" steady-state model to be used. Using steady-state techniques is particularly beneficial when assessing the effects of different parameter changes.

The accuracy of the developed steady-state model was confirmed by comparing it with transient finite-element simulations and experimental results when using a single sheet and a split-sheet with an electrodynamic wheel. Good agreement between the experimental results was obtained. The experimental results also helped to confirm the validity of a previously developed 2-D model.

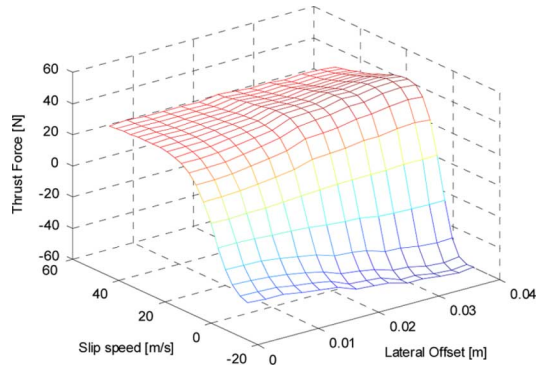

Fig. 35. Thrust force versus slip velocity and lateral rotor offset for a 5 ms^{-1} translational velocity.

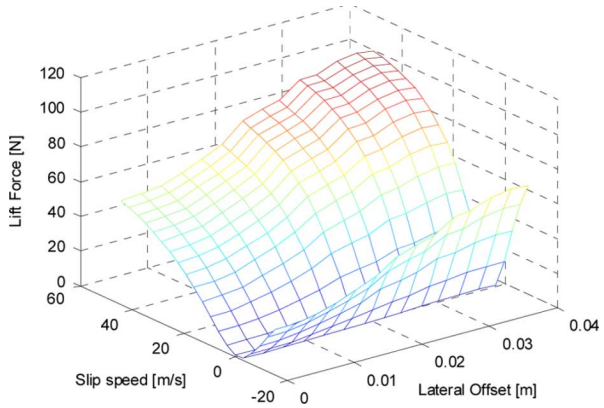

Fig. 36. Lift force versus slip velocity and lateral rotor offset for a 5 ms^{-1} translational velocity.

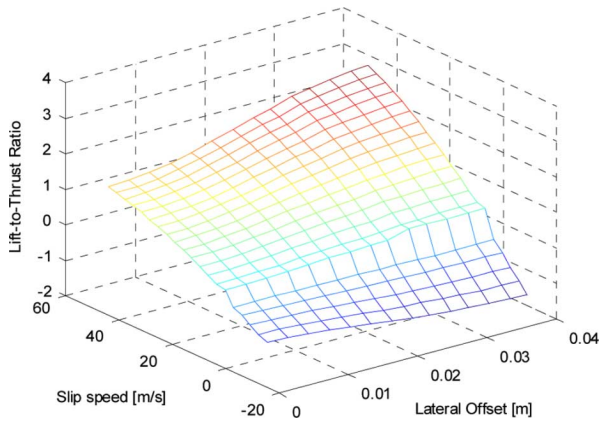

Fig. 37. Lift-to-thrust ratio versus slip velocity and lateral rotor offset for a 5 ms^{-1} translational velocity.

Although the designing and control of electrodynamic wheels for maglev transportation will be difficult, it has the potential to greatly reduce the cost of the maglev guideway.

ACKNOWLEDGMENT

The authors would like to acknowledge the support provided by the member companies of the Wisconsin Electric Machines and Power Electronics Consortium (WEMPEC) at the University of Wisconsin-Madison. Also, the authors would like to gratefully thank Dr. J. Hull at Argonne National Laboratories for providing the guideway wheel and the Magsoft Corporation for the use of their software.

REFERENCES

[1] G. H. Bohn and G. Steinmetz, "The electromagnetic levitation and guidance technology of the 'transrapid' test facility Emsland," *IEEE Trans. Magn.*, vol. MAG-20, no. 5, pp. 1666–1671, Sep. 1984.

[2] A. Cassat and M. Jufer, "MAGLEV projects technology aspects and choices," *IEEE Trans. Appl. Supercond.*, vol. 12, no. 1, pp. 915–925, Mar. 2002.

[3] K. R. Davey, "Designing with null flux coils," *IEEE Trans. Magn.*, vol. 33, no. 5, pp. 4327–4334, Sep. 1997.

[4] Proceedings of the Federal Transit Administration's Urban Maglev Workshop Federal Transit Administration, Washington, DC, Tech. Rep., Sep. 8–9, 2005.

[5] K. Karoly *et al.*, "Design considerations for the hunting and braking performance of Maglev vehicle utilzing permanent magnet EDS levitation system," in *Maglev' 2006*, Dresden, Germany, 2006, pp. 363–370.

[6] A. Stephan and A. Lascher, "Comparison of train resistances of transrapid and MLX01," in *MAGLEV 2004*, Shanghai, China, 2004, pp. 224–234.

[7] S. Wang *et al.*, "The man-loading high-temperature superconducting maglev test vehicle," *IEEE Trans. Appl. Supercond.*, vol. 13, no. 2, pp. 2134–2137, Jun. 2003.

[8] R. H. Borcherts and L. C. Davis, "The superconducting paddle-wheel as an integrated propulsion levitation machine for high speed ground transportation," *Electr. Mach. Electrom.*, vol. 3, pp. 341–355, Apr.–Jun. 1979.

[9] L. C. Davis and R. H. Borcherts, "Superconducting paddle wheels, screws, and other propulsion units for high-speed ground transportation," *J. Appl. Phys.*, vol. 44, pp. 3294–3299, Jul. 1973.

[10] M. Kawai and H. Ariga, "Equos-LIM-CAR," (in Japanese) *The Invention*, vol. 89, pp. 70–77, 1992.

[11] N. Fujii *et al.*, "Three dimensional force of magnet wheel with revolving permanent magnets," *IEEE Trans. Magn.*, vol. 33, no. 5, pp. 4221–4223, Sep. 1997.

[12] N. Fujii *et al.*, "Characteristics of magnetic lift, propulsion and guidance by using magnet wheels with rotating permanent magnets," in *IEEE Ind. Appl. Conf.*, 2000, pp. 257–262.

[13] N. Fujii *et al.*, "Basic characteristics of magnet wheels with rotating permanent magnets," in *IEEE Ind. Appl. Conf.*, 1994, pp. 203–209.

[14] N. Fujii *et al.*, "Revolving magnet wheels with permanent magnets," *Electr. Eng. Jpn.*, vol. 116, pp. 106–117, 1996.

[15] I. Boldea and S. A. Nasar, *Linear Motion Electromagnetic Systems*. New York: Wiley, 1985, pp. 461–478.

[16] Philco-Ford, "Department of Transportation, Conceptual Design and Analysis of the Tracked Magnetically Levitated Vehicle Technology Program (TMLV)—Repulse Scheme Volume 1—Technical Studies," Department of Transport, Springfield, VA, Tech. Rep. DOT-FR-40024 (Task I), Feb. 1975.

[17] J. Bird and T. A. Lipo, "An electrodynamic wheel: An integrated propulsion and levitation machine," in *Elect. Mach. Drives Conf.*, 2003, pp. 1410–1416.

[18] J. Bird and T. A. Lipo, "Calculating the forces created by an electrodynamic wheel using a 2-D steady-state finite-element model," *IEEE Trans. Magn.*, vol. 44, no. 3, Mar. 2008, to be published.

[19] J. Bird and T. A. Lipo, "Characteristics of an electrodynamic wheel using a 2-D steady-state model," *IEEE Trans. Magn.*, vol. 43, no. 8, pp. 3395–3405, Aug. 2007.

[20] J. Bird, "An investigation into the use of electrodynamic wheels for high-speed ground transportation," Ph.D. thesis, Dept. Electr. Eng., Univ. Wisconsin-Madison, Madison, WI, 2007.

[21] K. Halbach, "Design of permanent multipole magnets with oriented rare earth cobalt material," *Nucl. Instrum. Methods*, vol. 187, pp. 1–10, 1980.

[22] D. L. Atherton and A. R. Eastham, "Flat guidance schemes for magnetically levitated high-speed guided ground transport," *J. Appl. Phys.*, vol. 45, pp. 1398–1405, Mar. 1974.

[23] T. Sakamoto *et al.*, "Induced currents and forces for the split-guideway electrodynamic levitation system," *IEEE Trans. Magn.*, vol. 27, no. 6, pp. 5004–5006, Nov. 1991.

[24] Y. Iwasa, "Electromagnetic flight stability by model impedance simulation," *J. Appl. Phys.*, vol. 44, pp. 858–862, Feb. 1973.

[25] J. L. He and D. M. Rote, "Double-row loop-coil configuration for EDS maglev suspension, guidance, and electromagnetic guideway directional switching," *IEEE Trans. Magn.*, vol. 29, no. 6, pp. 2956–2958, Nov. 1993.

[26] *"Flux 2D Version 7.50 User Guide,"* Magsoft Corporation User Manual, Dec. 2000.

[27] *"Version 6.15 of MagNet,"* Infolytica Corporation, 2004.

[28] D. Rodger and H. C. Lai, "A comparison of formulations for 3-D finite-element modeling of electromagnetic launchers," *IEEE Trans. Magn.*, vol. 37, no. 1, pp. 135–138, Jan. 2001.

[29] B. T. Ooi, "A dynamic circuit theory of the repulsive magnetic levitation system," *IEEE Trans. Power App. Syst.*, vol. 96, no. 4, pp. 1094–1100, Jul. 1977.

[30] B. T. Ooi, "Electromechanical dynamics in superconducting levitation systems," *IEEE Trans. Magn.*, vol. MAG–11, no. 5, pp. 1495–1497, Sep. 1975.

[31] B. T. Ooi, "Electromechanical stiffness and damping coefficients in the repulsive magnetic levitation system," *IEEE Trans. Power App. Syst.*, vol. 95, no. 3, pp. 936–943, May/Jun. 1976.

[32] B. T. Ooi and O. P. Jain, "Force transients at guideway butt joints in repulsive magnetic levitation systems," *IEEE Trans. Power App. Syst.*, vol. PAS-98, no. 1, pp. 323–340, Jan./Feb. 1979.

[33] B. T. Ooi and O. P. Jain, "Moments and force densities of the electrodynamic levitation system," *IEEE Trans. Magn.*, vol. MAG-15, no. 3, pp. 1102–1108, May 1979.

[34] D. L. Atherton *et al.*, "Forces and moments for electrodynamic levitation systems—large-scale test results and theory," *IEEE Trans. Magn.*, vol. MAG-14, no. 2, pp. 59–68, Mar. 1978.

[35] K. Oberretl and N. Kratki, "Transients and oscillations in the repulsive magnetic levitation system," *IEEE Trans. Magn.*, vol. 11, no. 5, pp. 1493–1494, Sep. 1975.

[36] J. L. He *et al.*, "Applications of the dynamic circuit theory to maglev suspension systems," *IEEE Trans. Magn.*, vol. 29, no. 6, pp. 4153–4164, Nov. 1993.

[37] R. Knowles, "Dynamic circuit and fourier series methods for moment calculation in electrodynamic repulsive magnetic levitation systems," *IEEE Trans. Magn.*, vol. MAG-18, no. 4, pp. 953–960, Jul. 1982.

[38] A. R. Eastham and D. L. Atherton, "Superconducting linear synchronous motor propulsion and magnetic levitation for high speed ground transportation: Phase 3 interim report," Canadian Institute of Guided Ground Transport, Queen's University, Tech. Rep., 1976.

[39] J. L. He and H. T. Coffey, "Magnetic damping forces in figure-eight-shaped null-flux coil suspension systems," *IEEE Trans. Magn.*, vol. 33, no. 5, pp. 4230–4232, Sep. 1997.

[40] B. T. Ooi, "A generalized machine theory of the linear induction motor," *IEEE Trans. Power App. Syst.*, vol. PAS-92, pp. 1252–1259, Jul./Aug. 1973.

[41] D. G. Elliott, "Mesh-matrix analysis method for electromagnetic launchers," *IEEE Trans. Magn.*, vol. 25, no. 1, pp. 164–169, Jan. 1989.

[42] D. G. Elliott, Matrix analysis of linear induction machines U.S. Department of Transportation, Washington, D.C., Tech. Rep. FRA-OR&D-75-77, Sep. 1975.

[43] O. P. Jain, "Further applications of the dynamic circuit theory to the electrodynamic repulsive magnetic levitation systems," Ph.D. thesis, Dept. Elect. Eng., McGill Univ., Montreal, QC, Canada, 1978.

[44] J. Bird and T. A. Lipo, "Electrodynamic wheel and flat passive track topologies capable of creating lift, thrust and guidance forces simultaneously," presented at the 8th Int. Symp. Magnetic Suspension Technology, Dresden, Germany, 2005.

[45] D. Rodger *et al.*, "An optimal formulation for 3-D moving conductor eddy current problems with smooth rotors," *IEEE Trans. Magn.*, vol. 26, no. 5, pp. 2359–2363, Sep. 1990.

[46] D. K. Cheng, *Field and Wave Electromagnetics*. Reading, MA: Addison-Wesley, 1989.
[47] D. Kondrashov and D. Keefer, "A Maxwell's equation solver for 3-D MHD calculations," *IEEE Trans. Magn.*, vol. 33, no. 1, pp. 254–259, Jan. 1997.
[48] Y. Marechal *et al.*, "Computation of 3-D eddy currents in moving conductors of electromagnetic retarders," in *Proc. Int. Conf. Comp. Electro.*, London, U.K., Nov. 1991, pp. 25–27.
[49] H. Song and N. Ida, "Modeling of velocity terms in 3-D eddy current problems," *IEEE Trans. Magn.*, vol. 28, pp. 1178–1181, 1992.
[50] N. Ida, "Modeling of velocity effects in eddy current applications," *J. Appl. Phys.*, vol. 63, pp. 3007–3009, Apr. 15, 1988.
[51] K. Muramatsu *et al.*, "Method for analyzing eddy currents in moving conductors," *Electr. Eng. Jpn.*, vol. 114, pp. 102–113, Jul. 1994.
[52] D. Albertz *et al.*, "Calculation of the 3-D non-linear eddy current field in moving conductors and its application to braking systems," *IEEE Trans. Magn.*, vol. 32, no. 3, pp. 768–771, May 1996.
[53] C. R. I. Emson and J. Simkin, "An optimal method for 3-D eddy currents," *IEEE Trans. Magn.*, vol. 19, no. 6, pp. 2450–2452, Nov. 1983.
[54] D. Rodger and J. Eastham, "A formulation for low frequency eddy current solutions," *IEEE Trans. Magn.*, vol. 19, no. 6, pp. 2450–2452, Nov. 1983.
[55] D. Rodger *et al.*, "A formulation for 3-D moving conductor eddy current problems," *IEEE Trans. Magn.*, vol. 25, no. 5, pp. 4147–4149, Sep. 1989.
[56] S. Williamson and E. K. C. Chan, "Three-dimensional finite-element formulation for problems involving time-varying fields, relative motion, and magnetic saturation," *IEE Proc. A*, vol. 140, pp. 121–130, Mar. 1993.
[57] G. F. Carey and J. T. Oden, *Finite Elements: Fluid Mechanics Volume VI*. Englewood Cliffs, NJ: Prentice-Hall, 1986, p. 116.
[58] H. Goldstein *et al., Classical Mechanics*, p. 22, 2002.
[59] S. Yamamura, *Theory of Linear Induction Motors*. Tokyo, Japan: Univ. Tokyo Press, 1979, pp. 3–123.
[60] H. E. Knoepfel, *Magnetic fields: A Comprehensive Theoretical Treatise for Practical Use*. New York: Wiley, 2000.
[61] O. Biró and K. Preis, "On the use of the magnetic vector potential in the finite element analysis of three-dimensional eddy currents," *IEEE Trans. Magn.*, vol. 25, no. 4, pp. 3145–3159, Jul. 1989.
[62] S. Kurz *et al.*, "Numerical analysis of three-dimensional eddy current problems with moving boundaries by boundary element-finite-element method coupling," *Surv. Math. Ind*, pp. 131–150, 1999.
[63] R. D. Pillsbury, "A three dimensional eddy current formulation using two potentials: The magnetic vector potential and total magnetic scalar potential," *IEEE Trans. Magn.*, vol. 19, no. 6, pp. 2284–2287, Nov. 1983.
[64] E. K. C. Chan and S. Williamson, "Factors influencing the need for upwinding in two-dimensional field calculations," *IEEE Trans. Magn.*, vol. 28, no. 2, pp. 1611–1614, Mar. 1992.
[65] T. J. R. Hughes, "A simple scheme for developing 'upwind' finite elements," *Int. J. Numer. Methods Eng.*, vol. 12, pp. 1359–1365, 1978.
[66] T. J. R. Hughes, "Recent progress in the development and understanding of SUPG methods with special reference to the compressible Euler and Navier-Stokes equations," *Int. J. Numer. Methods Fluids*, vol. 7, pp. 1261–1275, Jul. 1987.
[67] T. J. R. Hughes and A. Brooks, "A theoretical framework for Petrov-Galerkin methods with discontinuous weighting functions: Application to the streamline-upwind procedure," in *Finite Elements in Fluids*, R. H. Gallagher, D. H. Norrie, J. T. Oden, and O. C. Zienkiewicz, Eds. New York: Wiley, 1982, vol. 4, pp. 47–66.
[68] T. J. R. Hughes *et al.*, "Streamline upwind/Petrov-Galerkin formulations for convection dominated flows with particular emphasis on the incompressible Navier-Stokes equations," *Comput. Methods Appl. Mech. Eng.*, vol. 32, pp. 199–259, Sep. 1982.
[69] O. C. Zienkiewicz and R. L. Taylor, *The Finite Element Method*, 4th ed. London, U.K.: McGraw-Hill, 1989, pp. 438–505.
[70] B. A. Finlayson, *Finite Element Handbook*, H. Kardestuncer, Ed., 1st ed. New York: McGraw-Hill, 1987.
[71] T. W. Preston and A. B. J. Reece, "Solution of 3-dimensional eddy current problems," *IEEE Trans. Magn.*, vol. MAG-18, no. 2, pp. 486–491, Mar. 1982.
[72] T. Nakata *et al.*, "Improvements of the T-Ω method for 3-D eddy current analysis," *IEEE Trans. Magn.*, vol. 24, no. 1, pp. 94–97, Jan. 1988.
[73] Y. Cai *et al.*, Dynamic stability of repulsive-force maglev suspension systems Argonne National Laboratory, Argonne, IL, Tech. Rep. ANL-96/18, 1996.

Manuscript received March 17, 2007; revised October 28, 2007. Corresponding author: J. Bird (e-mail: jonathan.bird@ieee.org).